Journal of ELECTRONIC MATERIALS, Vol. 47, No. 1, 2018
DOI: 10.1007/s11664-017-5790-4

RGO–RGONRs–Zn_2SnO_4 Composite with Three-Dimensional Hierarchical Structure for Use in Lithium-Ion Batteries

ZHAOHUI HOU,[1,2] ZHENGU CHEN,[1] MINGJUN JING,[1,3] HANG YANG,[1] GANGYONG LI,[1] and MINJIE ZHOU[1]

1.—College of Chemistry and Chemical Engineering, Hunan Institute of Science and Technology, Yueyang 414006, China. 2.—e-mail: zhaohuihou@126.com. 3.—e-mail: jingmingjun86@163.com

RGO–RGONRs–Zn_2SnO_4 composite with three-dimensional (3D) hierarchical structure has been formed from Zn_2SnO_4 nanoparticles grown on conducting reduced graphene oxide (RGO) and reduced graphene oxide nanoribbons (RGONRs) via a chemical co-reduction process. The presence of the RGONRs in this unique hybrid nanostructure prevents restacking of the graphene sheets and provides additional electron transport paths. Lithium-ion batteries using this 3D RGO–RGONRs–Zn_2SnO_4 composite as anode material displayed enhanced rate capability (510.6 mA h g^{-1} even at 1600 mA g^{-1}) and cycling properties (779.8 mA h g^{-1} after 50 cycles at current density of 200 mA g^{-1}).

Key words: Graphene oxide nanoribbons, RGO–RGONRs–Zn_2SnO_4, three-dimensional hierarchical structure, lithium-ion batteries

INTRODUCTION

Research has been focused on development of high-performance electrode materials to meet the increasing demand for lithium-ion batteries (LIBs) with enhanced energy/power density.[1,2] Tin-based oxides, such as SnO_2 and M_2SnO_4 (M = Zn, Co, Mn, Mg), have been actively investigated as potential anode materials for use in LIBs owing to their natural abundance and high theoretical capacity.[3–6] Zn_2SnO_4 is a tin-based oxide material with distinctive inverse spinel structure and has been widely studied in the field of LIBs.[5,7] The electrochemical reaction of Zn_2SnO_4 as an anode can be described based on the lithium storage mechanism of ZnO and SnO_2 as follows[3,4]:

$$4Li^+ + Zn_2SnO_4 + 4e^- \rightarrow Sn + 2Li_2O + 2ZnO \quad (1a)$$

$$8Li^+ + Zn_2SnO_4 + 8e^- \rightarrow 2Zn + Sn + 4Li_2O \quad (1b)$$

$$xLi^+ + Sn + xe^- \leftrightarrow Li_xSn, \ (x \leq 4.4) \quad (2)$$

$$yLi^+ + Zn + ye^- \leftrightarrow Li_ySn, \ (y \leq 1) \quad (3)$$

However, practical use of Zn_2SnO_4 in LIBs is hampered by its poor cycling stability. During the charge/discharge process, Zn_2SnO_4 anode material usually displays large volume expansion and severe particle aggregation.[8,9] Considerable effort has been applied to overcome these obstacles. Introduction of a carbon matrix into the Zn_2SnO_4 material is considered to be one effective method.[8,10,11]

Graphene, a two-dimensional (2D) carbon material, has attracted considerable attention due to its excellent conductivity, structural flexibility, ultrahigh theoretical surface area, and ultrathin thickness.[12,13] Many forms of hybrid material comprising tin-based oxides and graphene have been successfully manufactured, exhibiting improved electrical conductivity and cycling performance[3,4]; For example, a type of Zn_2SnO_4–graphene nanocomposite was prepared and showed reversible capacity of 688 mA h g^{-1} at current density of 200 mA g^{-1} after 50 cycles.[3] However, obtaining an ideal specific surface area and excellent conductivity is difficult due to the irreversible aggregation of graphene nanosheets.[14,15] Agglomeration of graphene is one of the most critical problems hindering its use as anode material. To solve these issues, use of one-

(Received April 3, 2017; accepted September 6, 2017; published online September 15, 2017)

dimensional (1D) carbon nanotubes (CNTs) has been proposed to physically separate the 2D graphene. Shen et al. produced a 3D TiO_2–graphene–CNT nanocomposite, where the CNTs can not only effectively avoid restacking of graphene, but can also result in an additional electron transport path for electrochemical processes. Compared with TiO_2–graphene composites, this 3D TiO_2–graphene–CNT nanocomposite exhibited enhanced electrochemical properties.[16]

Typical CNTs with length in the range of micrometers are highly tangled ropes. Owing to their structure with both ends closed, typical CNTs often have relatively low specific surface area, limiting their further application in the field of energy storage.[17,18] Graphene nanoribbons (GNRs) are excellent carbon materials that can be obtained by splitting multiwalled carbon nanotubes (MWCNTs), exhibiting high surface area, high carbon aspect ratio, and tunable electrical properties.[11,19,20] Given their good electrochemical properties, GNRs can be widely used in the energy sector. GNR–metal oxide composites have also been obtained for use as electrode materials in LIBs, exhibiting desirable capacity and rate performance.[21,22] Our previous study illustrated that LIBs with RGONRs–Zn_2SnO_4 as anode material displayed higher rate behavior and cycling stability compared with those using Zn_2SnO_4 nanoparticles.[23] Notably, GNRs, graphene, and metal oxide can form a special architecture; For example, a graphene–MnO_2–GNR composite with unique sandwich structure was successfully prepared, exhibiting enhanced capacity and cycling stability compared with graphene–MnO_2 composite and pure MnO_2 anode materials. Porous MnO_2 wrapped by graphene can be directly grown on GNRs in such a graphene–MnO_2–GNR composite.[24]

In this work, we designed a facile *in situ* hydrothermal approach to prepare a 3D reduced graphene oxide–reduced graphene oxide nanoribbons–Zn_2SnO_4 composite (RGO–RGONRs–Zn_2SnO_4). Similar to our previous report on RGONRs–Zn_2SnO_4,[23] Zn_2SnO_4 nanoparticles were grown on both 1D RGONRs and 2D RGO. Long RGONRs with high surface area could effectively bridge adjacent RGO, promoting electron transfer and inhibiting aggregation of RGO. This particular structure might be helpful to provide high contact area to facilitate electrolyte penetration and enhance the ion diffusion rate. LIBs using the 3D RGO–RGONRs–Zn_2SnO_4 composite as anode displayed enhanced electrochemical performance.

EXPERIMENTAL PROCEDURES

Synthesis of Samples

All chemical regents were of analytical grade and used without additional treatment. The length and diameter of the raw MWCNTs (Shenzhen Nanotech Port Co., Ltd.) were 5 μm to 15 μm and 60 nm to 100 nm, respectively. Graphite oxide (GO) was synthesized via a modified Hummers' method utilizing graphite flakes (99.8%; Alfa Aesar).[25]

The preparation of graphene oxide nanoribbons (GONRs) based on our previous report is briefly described below.[23] First, 0.15 g raw MWCNTs and 150 mL concentrated H_2SO_4 (98%) were mixed with stirring for 6 h at room temperature. Then, 700 mg $KMnO_4$ was added into this mixture at 65°C to split the walls and provide active edges. After heating for 2 h, 6 mL 30% H_2O_2 was further added into the above suspension in an ice bath for another 2 h. Finally, GONRs were obtained by washing with 10% HCl and deionized water.

RGO–RGONRs–Zn_2SnO_4 composite was manufactured using a simple hydrothermal process. First, GO–GONRs suspension was obtained by mixing 40 mg GONRs and 40 mg GO under ultrasonic treatment for 2 h in deionized water. Subsequently, 0.1363 g $ZnCl_2$ and 0.1753 g $SnCl_4{\cdot}5H_2O$ were both dissolved in deionized water. Then, this solution was added dropwise into the as-obtained GO–GONRs suspension while stirring. Subsequently, 245 μL $N_2H_4{\cdot}H_2O$ was directly added, followed by stirring for another 0.5 h. The as-obtained mixture was poured into a Teflon-lined stainless-steel autoclave and further treated for 24 h at 180°C. After natural cooling, the sediment was isolated by centrifugation, then washed with deionized water, and dried at 60°C for 12 h. Finally, the RGO–RGONRs–Zn_2SnO_4 product was prepared by annealing under Ar atmosphere at 500°C for 2 h with heating rate of 10°C/min.

RGO–Zn_2SnO_4 composite and pure Zn_2SnO_4 nanoparticles were both obtained under similar experimental conditions in absence of GONRs or GO–GONRs.

Materials Characterization

X-ray diffraction (XRD) analysis (D/max-Ultima IV) was utilized to investigate the crystalline structure of RGO–RGONRs–Zn_2SnO_4 and pure Zn_2SnO_4. Scanning electron microscopy (SEM, JSM-6510LV) and transmission electron microscopy (TEM, JEM-2100F) were used to analyze the morphology and microstructure of the samples. The specific surface area of the samples was analyzed via nitrogen adsorption–desorption isotherms (Micromeritics ASAP 2020 analyzer) obtained at 77 K. The composition of the samples was further investigated using thermogravimetric analysis (TGA, DTA7300, JEOL Ltd.) from room temperature to 800°C at 10°C/min under air.

Electrochemical Characterization

Active material, acetylene black, and polyvinylidene fluoride binder (weight ratio 80:10:10) were dissolved in *N*-methyl-2-pyrrolidinone (NMP) to prepare the working electrodes. The obtained slurries were then uniformly painted on pure copper

foil. After drying at 80°C in vacuum for 10 h and pressing under pressure of approximately 20 MPa, electrode disks (12 mm diameter) were obtained with dry coating thickness of approximately 80 μm and mass loading of 1.5 mg to 1.8 mg. CR2025 coin-type cells were assembled in an argon-filled glovebox with lithium foil as counter and reference electrodes, and microporous polypropylene as separator. The electrolyte used was solution of $LiPF_6$ (1 M) in ethylene carbonate/ethyl methyl carbonate/dimethyl carbonate (1:1:1, v/v/v). Galvanostatic charge/discharge measurements of RGO–Zn_2SnO_4 and RGO–RGONRs–Zn_2SnO_4 composite were carried out using a LAND battery tester in the voltage range from 0.005 V to 3 V (versus Li/Li^+) at various rates. Electrochemical impedance spectroscopy (EIS) was carried out using an electrochemical working station (CHI 660B, Shanghai Chenhua Instrument Factory) after the cells were discharged and charged for three cycles in the frequency range from 100 kHz to 0.01 Hz.

RESULTS AND DISCUSSION

A schematic of the assumed formation processes of the RGO–RGONRs–Zn_2SnO_4 composite is shown in Scheme 1. First, highly dispersed GONRs were prepared via a $KMnO_4$ solution-based oxidative process via lengthwise unzipping of MWCNT sidewalls. The GO sample was synthesized using a modified Hummers' method. Subsequently, appropriate amounts of $ZnCl_2$ and $SnCl_4{\cdot}5H_2O$ were added into the GO–GONRs solution. Based on the abundant oxygenic groups on the surface of GO–GONRs,[3,11] researchers have found that Zn^{2+} and Sn^{4+} cations can be homogeneously deposited on GO–GONRs. Notably, GO and GONRs could also be reduced through *in situ* chemical co-reduction. Finally, RGO–RGONRs–Zn_2SnO_4 composite with 3D structure was obtained. Due to the high specific surface area of the GO–GONRs, the as-prepared Zn_2SnO_4 particles could be homogeneously detached and immobilized on the surface of RGO–RGONRs.

The crystalline structure of the as-obtained RGO–RGONRs–Zn_2SnO_4 and pure Zn_2SnO_4 samples was investigated by XRD analysis, as shown in Fig. 1. All of the diffraction peaks observed for pure Zn_2SnO_4 could be definitely indexed to cubic Zn_2SnO_4 according to Joint Committee on Powder Diffraction Standards (JCPDS) card no. 74-2184.[3] An additional small diffraction peak at 2θ of 25.2° could be indexed to RGO and RGONRs.[26] This small peak for the RGO–RGONRs–Zn_2SnO_4 composite was not clearly observed, possibly due to the low weight fraction and noncrystalline structure of RGO–RGONRs.

Figure 2 shows SEM and TEM images of the samples. Pure Zn_2SnO_4 prepared in absence of GO–GONRs exhibited spherical nanoparticle morphology with approximate size of 25 nm (Fig. 2a).

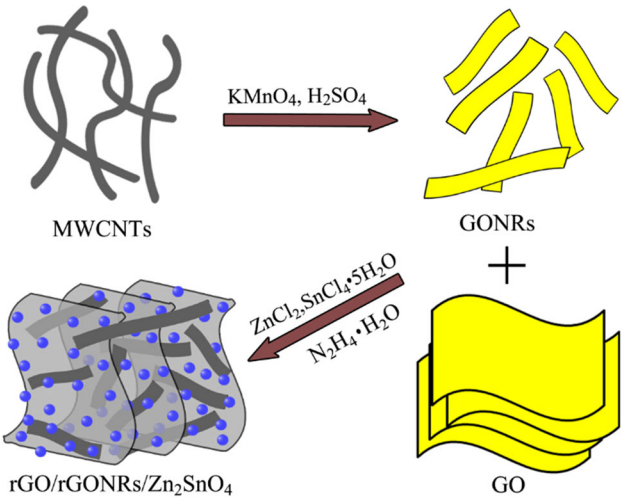

Scheme 1. Scheme for synthesis of RGO–RGONRs–Zn_2SnO_4 composite.

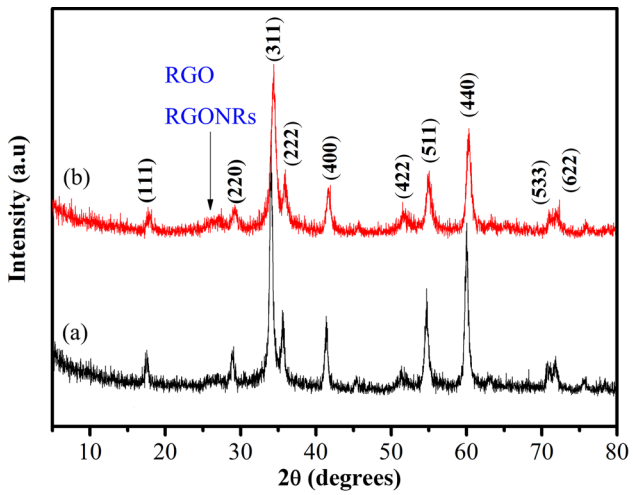

Fig. 1. XRD patterns of (a) pure Zn_2SnO_4 and (b) RGO–RGONRs–Zn_2SnO_4 composite.

Figure 2b shows ribbon-like graphene structures, suggesting that MWCNTs were successfully unzipped using the advanced oxidation process. The GONRs had width of approximately 130 nm, exhibiting larger accessible area. Moreover, Fig. 2c and d presents typical SEM micrographs of the RGO–RGONRs–Zn_2SnO_4 composite. RGO–RGONRs–Zn_2SnO_4 composite with 3D structure was successfully prepared. Spherical Zn_2SnO_4 particles were homogeneously anchored onto the RGO–RGONRs surface. In addition, TEM images of the RGO–RGONRs–Zn_2SnO_4 composite were also obtained and are shown in Fig. 2e and f. Spherical Zn_2SnO_4 with size of ~25 nm was well dispersed on the 3D network of the RGO–RGONRs, which can be attributed to the strong interaction between Zn_2SnO_4 particles and RGO–RGONRs. Notably,

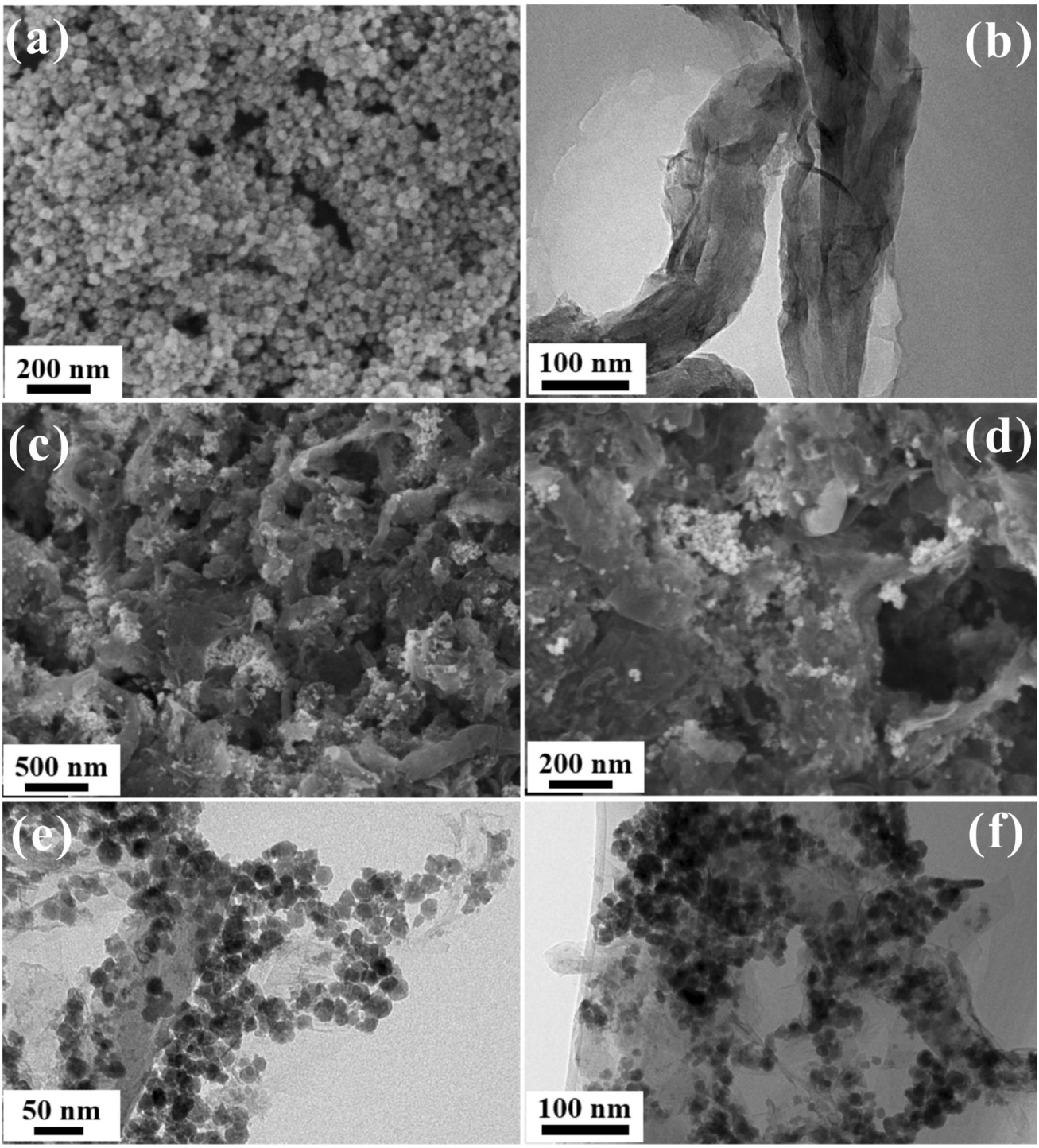

Fig. 2. (a) SEM image of bare Zn_2SnO_4 nanoparticles, (b) TEM image of pure RGONRs, and (c, d) SEM and (e, f) TEM images of RGO–RGONRs–Zn_2SnO_4 composite.

the π–π interaction between the graphene sheets could also be effectively reduced due to steric hindrance during the hydrothermal process. Thereby, aggregation of the Zn_2SnO_4 nanoparticles could be prevented with the abundant pores formed in the 3D hierarchical structure.[16]

Figure 3 displays the TGA analysis of RGO–Zn_2SnO_4 and RGO–RGONRs–Zn_2SnO_4 from 35°C to 800°C under air atmosphere. The initial weight loss below 100°C can be attributed to loss of moisture or gases absorbed on the surface of the samples. The second weight loss from 100°C to

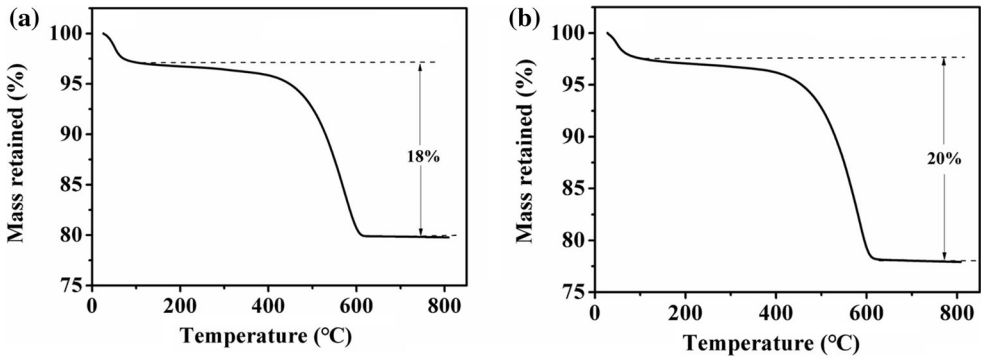

Fig. 3. TGA curves of (a) RGO–Zn_2SnO_4 composite and (b) RGO–RGONRs–Zn_2SnO_4 composite.

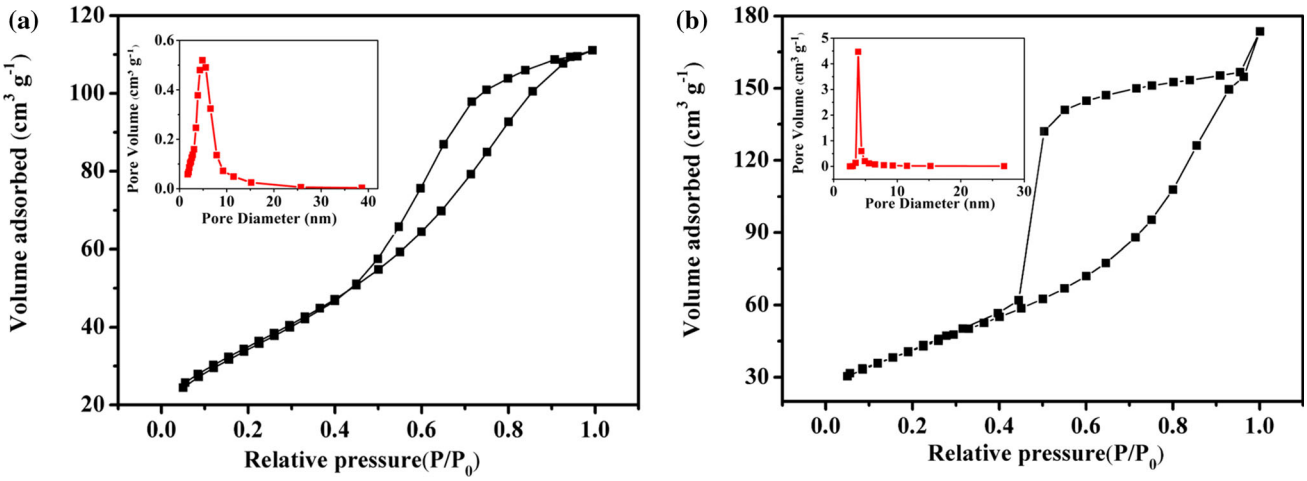

Fig. 4. Nitrogen adsorption/desorption isotherms of (a) RGO–Zn_2SnO_4 and (b) RGO–RGONRs–Zn_2SnO_4 composites, with pore size distributions calculated by BJH method (inset).

600°C can be ascribed to oxidization of carbon materials. The curves for both samples are rather stable at temperatures above 600°C, indicating that both RGO and RGONRs completely disappeared.[27] Based on these results, the quantity of RGO in the RGO–Zn_2SnO_4 composite was approximately 18%, while the amount of RGO–RGONRs in the RGO–RGONRs–Zn_2SnO_4 composite was approximately 20%.

The N_2 absorption/desorption isotherms of the RGO–Zn_2SnO_4 and RGO–RGONRs–Zn_2SnO_4 samples are shown in Fig. 4. The Brunauer–Emmet–Teller specific surface area of the RGO–RGONRs–Zn_2SnO_4 sample was measured to be 149.87 $m^2\ g^{-1}$, obviously higher than that of the RGO–Zn_2SnO_4 composite (128.40 $m^2\ g^{-1}$), indicating that addition of RGONRs resulted in a larger specific surface area for the material. The pore size distribution curves obtained based on the Barrett–Joyner–Halenda method are shown in the inset of Fig. 4. The total pore volume of the RGO–Zn_2SnO_4 and RGO–RGONRs–Zn_2SnO_4 composites was 0.203 $cm^3\ g^{-1}$ and 0.324 $cm^3\ g^{-1}$, respectively. The enhanced pore volume of the RGO–RGONRs–Zn_2SnO_4 composite material can be ascribed to formation of secondary pores among Zn_2SnO_4, RGONRs, and RGO.[28] Notably, this kind of porous nanostructure and high specific surface area suggests a highly conductive medium for electron transfer with shortened diffusion paths of Li^+.[29]

Figure 5a and b show typical discharge–charge voltage curves for the RGO–Zn_2SnO_4 and RGO–RGONRs–Zn_2SnO_4 composites obtained in the potential range from 0.005 V to 3 V at current density of 200 mA g^{-1}. The first discharge and charge specific capacities of the RGO–RGONRs–Zn_2SnO_4 composite electrode were 1764.5 mA h g^{-1} and 938.8 mA h g^{-1}, while the first discharge and charge specific capacities of the RGO–Zn_2SnO_4 composite were 1325.3 mA h g^{-1} and 659.6 mA h g^{-1}. The first coulombic efficiencies of RGO–RGONRs–Zn_2SnO_4 and RGO–Zn_2SnO_4 were 53.2% and 49.7%, respectively. Both initial capacity losses can be mainly attributed to irreversible electrolyte decomposition and unavoidable formation of solid electrolyte interphase (SEI) films.[30] Notably, the capacity and first coulombic efficiency of the RGO–RGONRs–Zn_2SnO_4 composite were

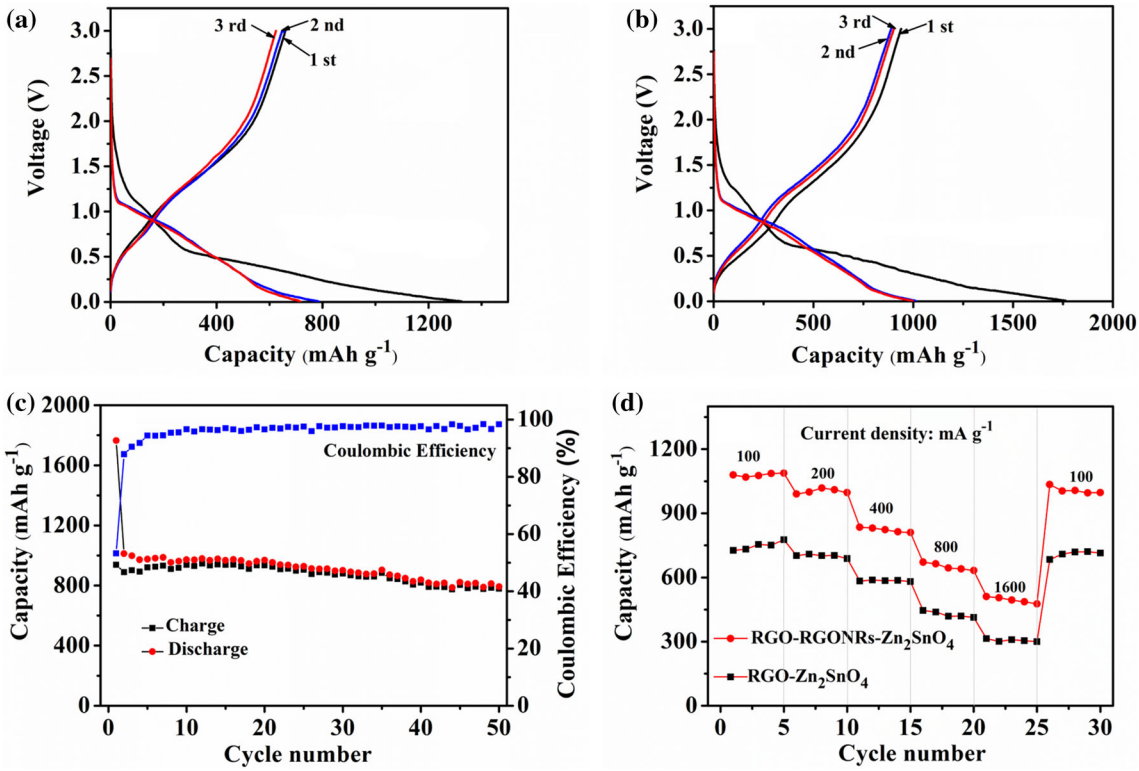

Fig. 5. Voltage profiles of (a) RGO–Zn_2SnO_4 and (b) RGO–RGONRs–Zn_2SnO_4 composites when charged/discharged at 200 mA g^{-1}, (c) cycling performance and coulombic efficiency of RGO–RGONRs–Zn_2SnO_4 composite at 200 mA g^{-1}, and (d) rate capability of RGO–Zn_2SnO_4 and RGO–RGONRs–Zn_2SnO_4 composites.

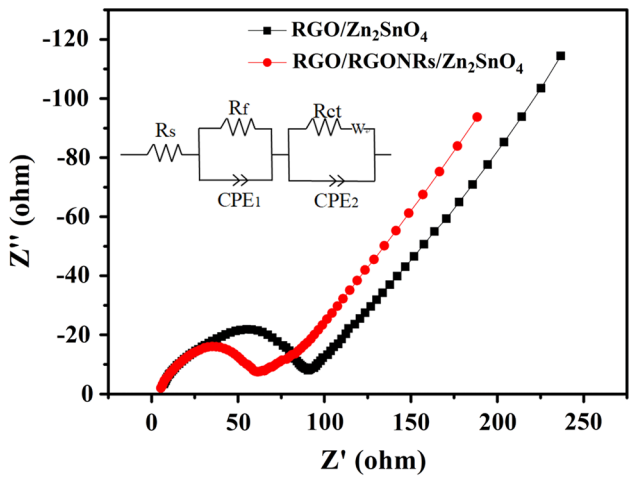

Fig. 6. EIS results for RGO–Zn_2SnO_4 and RGO–RGONRs–Zn_2SnO_4 composite electrodes after three cycles.

both much higher than those of the RGO–Zn_2SnO_4 composite. During subsequent cycles, the RGO–RGONRs–Zn_2SnO_4 electrode exhibited much higher electrochemical performance for lithium storage compared with the RGO–Zn_2SnO_4 electrode, suggesting that more lithium insertion/extraction sites existed in the RGO–RGONRs–Zn_2SnO_4 composite. Though the content of Zn_2SnO_4 in RGO–RGONRs–Zn_2SnO_4 was lower than that in RGO–Zn_2SnO_4, the specific surface area of RGO–RGONRs–Zn_2SnO_4 was much larger than that of RGO–Zn_2SnO_4. The larger charge capacity of the RGO–RGONRs–Zn_2SnO_4 composite electrode might therefore be ascribed to a synergetic effect between RGO–Zn_2SnO_4 and the conductive RGONRs. On the one hand, the 3D hierarchical structure of RGO–RGONRs–Zn_2SnO_4 could be formed with the introduction of conductive RGONR wraps, improving lithium-ion diffusion processes. On the other hand, more active sites of RGO–RGONRs–Zn_2SnO_4 could participate in the electrochemical reaction owing to the larger specific surface area of RGO–RGONRs–Zn_2SnO_4.

Figure 5c shows the capacity retention performance of the RGO–RGONRs–Zn_2SnO_4 composite at current density of 200 mA g^{-1}. This composite maintained reversible charge capacity of 779.8 mA h g^{-1} after 50 cycles, which is higher than other previously reported Zn_2SnO_4-based nanocomposites.[3,4,7,23] The coulombic efficiency of the RGO–RGONRs–Zn_2SnO_4 composite was above 90% after three cycles, and remained at 98.3% after 50 cycles. In addition, the rate performance of the RGO–Zn_2SnO_4 and RGO–RGONRs–Zn_2SnO_4 composites at different current densities from 100 mA g^{-1} to 1600 mA g^{-1} was also studied (Fig. 5d). The specific capacity of the RGO–

RGONRs–Zn_2SnO_4 electrode was 1069.2 mA h g^{-1}, 999.1 mA h g^{-1}, 830.9 mA h g^{-1}, 671.7 mA h g^{-1}, and 510.6 mA h g^{-1} at current density of 100 mA g^{-1}, 200 mA g^{-1}, 400 mA g^{-1}, 800 mA g^{-1}, and 1600 mA g^{-1}, respectively, being much higher than the values for RGO–Zn_2SnO_4. Moreover, this rate behavior is much better than that of RGONRs–Zn_2SnO_4 (330.4 mA h g^{-1} at 1600 mA g^{-1}), as demonstrated in our previous report.[23] The charge capacity of the RGO–RGONRs–Zn_2SnO_4 composite recovered to 957 mA h g^{-1}, close to the original capacity, when the current density went back to 100 mA g^{-1}, indicating excellent electrochemical stability of this RGO–RGONRs–Zn_2SnO_4 electrode for lithium storage during cycling.[10,31] The improved cycling ability and high rate performance of the RGO–RGONRs–Zn_2SnO_4 composite can be ascribed to the following effects: First, RGONRs as conductive wires can connect well with graphene sheets, further increasing the specific surface area and improving the conductivity of the composite[32,33]; Second, the 3D network composed of RGONRs and RGO can effectively diminish the π–π interaction between graphene sheets, hence the degree of restacking of RGO could be reduced, resulting in many more active sites for lithium storage; Last but not least, the 3D hierarchical architecture of the RGO–RGONRs could not only provide a support for anchoring well-dispersed Zn_2SnO_4 nanoparticles, but can also act as a mechanical buffer that can relieve the volume expansion of Zn_2SnO_4 during cycling.[11,23]

To evaluate the improvement of the electronic conductivity of the RGO–RGONRs–Zn_2SnO_4 composite with the introduction of RGO–RGONRs, EIS measurements were performed. EIS analysis of the RGO–Zn_2SnO_4 and RGO–RGONRs–Zn_2SnO_4 electrodes was carried out at open-circuit voltage from 0.01 Hz to 100 kHz after three cycles, and the results are displayed in Fig. 6. The impedance curves for both samples were composed of a wide semicircle and a straight sloping line. The semicircle in the high–medium frequency region can be attributed to the charge-transfer impedance (R_{ct}) at the electrode–electrolyte interface,[23] while the inclined line can be ascribed to the Warburg impedance (W) of the mass-transfer-controlled Warburg area.[34] Compared with the curve for the RGO–Zn_2SnO_4 electrode (Fig. 6), the EIS results for the RGO–RGONRs–Zn_2SnO_4 electrode displayed a much smaller diameter and steeper and straighter slope, illustrating that the RGO–RGONRs–Zn_2SnO_4 composite exhibited lower charge-transfer resistance and faster electron transportation by diffusion. The electrical conductivity of RGO–RGONRs–Zn_2SnO_4 was therefore successfully enhanced by the introduction of RGONRs, further illustrating the improved electrochemical performance of the RGO–RGONRs–Zn_2SnO_4 composite for lithium storage.

CONCLUSIONS

A RGO–RGONRs–Zn_2SnO_4 composite with 3D structure was successfully prepared via a simple *in situ* chemical co-reduction method. Zn_2SnO_4 nanoparticles could be uniformly attached to the 3D network of the RGO–RGONRs, which is beneficial to enhance the high rate performance. With the introduction of highly conductive RGO–RGONRs, this composite can serve as an ideal host for fast and efficient lithium storage. The RGO–RGONRs–Zn_2SnO_4 composite with 3D architecture showed high rate behavior with capacity of 510.6 mA h g^{-1} even at current density of 1600 mA g^{-1} and good cycling stability with capacity of 779.8 mA h g^{-1} at 200 mA g^{-1} after 50 cycles.

ACKNOWLEDGEMENTS

This work was supported by the National Natural Science Foundation of China (No. 51372080), the Natural Science Foundation of Hunan Province, China (Grant No. 2017JJ3097), and the Research Foundation of Education Bureau of Hunan Province, China (Grant Nos. 17A086, 16C0717, and 17K039). We gratefully acknowledge Professor Xu-Biao Luo (Nanchang Hangkong University) and Dr. Fan-Yan Zeng (Jiangxi Normal University) for help with XRD, SEM, and TEM.

REFERENCES

1. K.T. Nam, D.W. Kim, P.J. Yoo, C.Y. Chiang, N. Meethong, P.T. Hammond, Y.-M. Chiang, and A.M. Belcher, *Science* 312, 885 (2006).
2. J.B. Goodenough and K.S. Park, *J. Am. Chem. Soc.* 135, 1167 (2013).
3. W. Song, J. Xie, W. Hu, S. Liu, G. Cao, T. Zhu, and X. Zhao, *J. Power Sources* 229, 6 (2013).
4. H. Huang, Y. Huang, M. Wang, X. Chen, Y. Zhao, K. Wang, and H. Wu, *Electrochim. Acta* 147, 201 (2014).
5. Y.R. Lim, C.S. Jung, H.S. Im, K. Park, J. Park, W.I. Cho, and E.H. Cha, *J. Mater. Chem. A* 4, 10691 (2016).
6. F. Han, W.-C. Li, M.-R. Li, and A.-H. Lu, *J. Mater. Chem.* 22, 9645 (2012).
7. W. Song, J. Xie, S. Liu, G. Cao, T. Zhu, and X. Zhao, *J. Mater. Res.* 27, 3096 (2012).
8. K. Wang, Y. Huang, Y. Shen, L. Xue, H. Huang, H. Wu, and Y. Wang, *Ceram. Int.* 40, 15183 (2014).
9. W.S. Yuan, Y.W. Tian, and G.Q. Liu, *J. Alloys Compd.* 506, 683 (2010).
10. C. Yan, J. Yang, Q. Xie, Z. Lu, B. Liu, C. Xie, S. Wu, Y. Zhang, and Y. Guan, *Mater. Lett.* 138, 120 (2015).
11. J. Lin, Z. Peng, C. Xiang, G. Ruan, Z. Yan, D. Natelson, and J.M. Tour, *ACS Nano* 7, 6001 (2013).
12. G. Zhou, D.W. Wang, L.C. Yin, N. Li, F. Li, and H.M. Cheng, *ACS Nano* 6, 3214 (2012).
13. G. Sun, X. Zhang, R. Lin, J. Yang, H. Zhang, and P. Chen, *Angew. Chem.* 127, 4734 (2015).
14. F. Zeng, Y. Kuang, N. Zhang, Z. Huang, Y. Pan, Z. Hou, H. Zhou, C. Yan, and O.G. Schmidt, *J. Power Sources* 247, 396 (2014).
15. Y. Si, *Nano Lett.* 8, 1679 (2008).
16. L. Shen, X. Zhang, H. Li, C. Yuan, and G. Cao, *J. Phys. Chem. Lett.* 2, 3096 (2011).
17. L. Chen, H. Zhou, S. Wei, Z. Chen, Z. Huang, Z. Huang, C. Zhang, and Y. Kuang, *RSC Adv.* 5, 8175 (2015).
18. Y. Cheng, S. Lu, H. Zhang, C.V. Varanasi, and J. Liu, *Nano Lett.* 12, 4206 (2012).
19. B. Luo, S. Liu, and L. Zhi, *Small* 8, 630 (2012).

20. B. Genorio, W. Lu, A.M. Dimiev, Y. Zhu, A.-R.O. Raji, B. Novosel, L.B. Alemany, and J.M. Tour, *ACS Nano* 6, 4231 (2012).
21. J. Lin, A.-R.O. Raji, K. Nan, Z. Peng, Z. Yan, E.L.G. Samuel, D. Natelson, and J.M. Tour, *Adv. Funct. Mater.* 24, 2044 (2014).
22. Y. Yang, L. Li, H. Fei, Z. Peng, G. Ruan, and J.M. Tour, *ACS Appl. Mater. Int.* 6, 9590 (2014).
23. M. Jing, Z. Hou, H. Yang, G. Li, M. Zhou, and W. Xu, *J. Mater. Res.* 31, 3666 (2016).
24. L. Li, A.R. Raji, and J.M. Tour, *Adv. Mater.* 25, 6298 (2013).
25. W.S. Hummers and R.E. Offeman, *J. Am. Chem. Soc.* 80, 1339 (1958).
26. Y. Yang, L. Li, H. Fei, Z. Peng, G. Ruan, and J.M. Tour, *ACS Appl. Mater. Int.* 6, 9590 (2014).
27. Y. Dou, J. Xu, B. Ruan, Q. Liu, Y. Pan, Z. Sun, and S.X. Dou, *Adv. Energy Mater.* 6, 1501835 (2016).
28. H.Y. Wang, B.Y. Wang, J.K. Meng, J.G. Wang, and Q.C. Jiang, *J. Mater. Chem. A* 3, 1023 (2015).
29. Y. Zhao, Y. Huang, X. Sun, H. Huang, K. Wang, M. Zong, and Q. Wang, *Electrochim. Acta* 120, 128 (2014).
30. Y. Zhao, Y. Huang, Q. Wang, K. Wang, M. Zong, L. Wang, W. Zhang, and X. Sun, *RSC Adv.* 3, 14480 (2013).
31. A. Rong, X.P. Gao, G.R. Li, T.Y. Yan, H.Y. Zhu, J.Q. Qu, and D.Y. Song, *J. Phys. Chem. B* 110, 14754 (2006).
32. Q. Peng, Y. Li, X. He, X. Gui, Y. Shang, C. Wang, C. Wang, W. Zhao, S. Du, E. Shi, P. Li, D. Wu, and A. Cao, *Adv. Mater.* 26, 3241 (2014).
33. A.L. Higginbotham, D.V. Kosynkin, A. Sinitskii, Z. Sun, and J.M. Tour, *ACS Nano* 4, 2059 (2010).
34. D. Yin, G. Huang, Q. Sun, Q. Li, X. Wang, D. Yuan, C. Wang, and L. Wang, *Electrochim. Acta* 215, 410 (2016).